Martinez Garzon, P., Durand, V., Bentz, S., Kwiatek, G., Dresen, G., Turkmen, T., Nurlu, M., Bohnhoff, M. (2021): Near-Fault Monitoring Reveals Combined Seismic and Slow Activation of a Fault Branch within the Istanbul–Marmara Seismic Gap in Northwest Turkey. - Seismological Research Letters, 92, 6, 3743-3756.

https://doi.org/10.1785/0220210047

Near-fault monitoring reveals combined seismic and slow activation of a fault branch within the Istanbul-Marmara seismic gap in NW Turkey

Patricia Martínez-Garzón[1], Virginie Durand[1], Stephan Bentz[1], Grzegorz Kwiatek[1], Georg Dresen[1,2], Taylan Turkmen[3], Murat Nurlu[4], Marco Bohnhoff[1,5]

1. Helmholtz Centre Potsdam, GFZ German Research Centre for Geosciences, Section 4.2: Geomechanics and Scientific Drilling, Telegrafenberg, 14473 Potsdam, Germany
2. University of Potsdam, Institute of Earth and Environmental Sciences, Potsdam, German
3. AFAD Yalova Disaster and Emergency Management Authority Turkey, Yalova, Turkey.
4. AFAD Disaster and Emergency Management Authority Turkey, Ankara, Turkey.
5. Free University Berlin, Institute of Geological Sciences, Berlin, Germany.

Corresponding author:

Patricia Martínez-Garzón, Helmholtz Centre Potsdam, GFZ German Research Centre for Geosciences, Section 4.2: Geomechanics and Scientific Drilling, Telegrafenberg, 14473 Potsdam, Germany (patricia@gfz-potsdam.de)

Seismological Research Letters, 2021

Declaration of interest: The authors acknowledge there are no conflict of interests recorded.

Key points:

- We combine microseismicity and strainmeter recordings to propose the mechanisms driving the episodic micro-seismicity framing a M_W 4.5 earthquake and subsequent slow slip in the eastern Marmara region in 2018.
- Different properties of the seismic events together with the observed slow signal after the M_W 4.5 suggest that the episodic seismicity during the following year is mainly controlled by a superposition of slow slip, fluid migration along the fault and stress loading of remaining asperities.
- Our findings are the second observation in this area of transient slow slip using strainmeters occurring in the framework of enhanced local seismic moment release, highlighting the coexistence and interaction of seismic and aseismic deformation in the eastern Sea of Marmara region where a M7+ earthquake is overdue.

Abstract

Various geophysical observations show that seismic and aseismic slip on a fault may occur concurrently. We analyze microseismicity recordings from a temporary near-fault seismic network and borehole strainmeter data from the eastern Marmara region in NW Turkey to track seismic and aseismic deformation around the hypocentral region of a M_W 4.5 earthquake in 2018. A slow transient is observed that lasted about 30 days starting at the time of the M_W 4.5 event. We study about 1,200 microseismic events that occurred during 417 days after the M_W 4.5 event around the mainshock fault rupture. The seismicity reveals a strong temporal clustering, including four episodic seismic sequences each containing more than 30 events per day. Seismicity from the first two sequences displayed typical characteristics driven by aseismic slip and/or fluids, such as the activation of a broader region around the mainshock, and swarm-like topology. The third and fourth sequences correspond to typical mainshock-aftershock sequences. These observations suggest that slow slip and potentially fluid diffusion along the fault plane could have controlled the seismicity during the initial 150 days following the M_W 4.5 event. In contrast, stress redistribution and breaking of remaining asperities may have caused the activity after the initial 150 days. Our observation from a newly installed combined dense seismic and borehole strainmeter network follows an earlier observation of a slow transient occurring in conjunction with enhanced local seismic moment release in the same region. This suggests a frequent interaction of seismic and aseismic slip in the Istanbul-Marmara seismic gap.

Introduction

In recent years, integrated analysis of seismic and geodetic data covering a broad frequency range has provided expanding evidence for the relevance of aseismic deformation during most stages of the seismic cycle (e.g. Peng & Gomberg, 2010). Prior to large stick-slip failure, laboratory rock deformation experiments show a phase of combined seismic and aseismic deformation surrounding faults stressed close to failure (e.g. Dresen et al., 2020). On the field scale, slow or aseismic transients have been detected before megathrust earthquakes such as the M_W 9.1 2011 Tohoki-Oki earthquake (Mavrommatis et al., 2014), but also prior to small earthquakes such as a M_W 3.7 event in central Alaska (Tape et al., 2018). After an earthquake, the hypocentral region releases postseismic deformation combining afterslip and viscoelastic relaxation processes at varying depth and time scales from days to years (e.g. Wang et al., 2012). Continuous fault slip after an earthquake termed afterslip has been documented as a main mechanism driving earthquake aftershock sequences following mainshocks of various magnitudes. These include large strike-slip earthquakes such as the M_W 7.4 1999 Landers in the Eastern Californian Shear Zone (Perfettini & Avouac, 2004), megathrusts such as the M_W 8.8 2010 Maule earthquake in Chile (Bedford et al., 2013), intermediate magnitude earthquakes such as the M_W 5.8 2010 Collins Valley earthquake at the strike-slip San Jacinto Fault (Inbal et al., 2017), the normal faulting M_W 5.7 2020 Magna earthquake along the Wasatch Fault Zone (Pollitz et al., 2021), and several M>4 earthquakes along the San Andreas Fault in central California (Hawthorne et al., 2016). In addition, static or dynamic stress changes have been observed to triggered slow slip of varying sizes (e.g. Taira et al., 2014; Rolandone et al., 2018). As triggered slow slip events release accumulated tectonic strain (Burgmann, 2018), their detection is crucial for estimating elastic strain accumulated along a fault zone and hence to assess its seismic hazard. This is particularly important for fault zones running near dense population centers that carry a larger seismic risk.

The North Anatolian Fault Zone (NAFZ) in Turkey runs onshore for almost 1000 km until it enters the Sea of Marmara region. Directly east of the Marmara region, the M_W 7.4 Izmit earthquake in 1999 caused more than 18.000 fatalities (e.g., Barka et al., 2002). Its rupture extended into the Sea of Marmara triggering numerous aftershocks on the Armutlu Peninsula south of Istanbul. Currently, the NAFZ segment below the Sea of Marmara is late in its seismic cycle and a M>7 earthquake during the next decades is expected (Parsons, 2004; Murlu et al., 2016; Bohnhoff et al., 2013; 2016). The direct proximity to the Istanbul metropolitan region translates the seismic hazard into high seismic risk affecting > 15 million inhabitants and key infrastructure. In this setting, near-fault monitoring is required to generate high-resolution microseismicity catalogs, resolve mechanisms driving the seismicity, identify locked patches possibly representing nucleation spots of future mainshocks, and to optimize preconditions for earthquake-early warning. To that end, the permanent downhole geophysical observatory GONAF (Bohnhoff et al., 2017) is operating in the eastern Marmara region since 2015, monitoring seismicity at low magnitude detection threshold and capturing the entire width of deformation processes using borehole seismometers and strainmeters (e.g. Martínez-Garzón et al., 2019). In 2019-2020, near-fault monitoring was further improved along the only onshore portion of the Marmara seismic gap by the installation of a local dense temporary seismic network on the Armutlu Peninsula south of Istanbul (SMARTnet).

In this study, we discuss the crustal deformation along the northern Armutlu Peninsula following the occurrence of a local M_W 4.5 earthquake that occurred on a fault nearly perpendicular to the Cinarcik fault branch of the NAFZ. We generated a new local microseismicity catalog of unprecedented resolution for the region utilizing the continuous recordings provided by the SMARTnet and GONAF monitoring infrastructure and investigated the spatio-temporal features, migration patterns and kinematic characteristics of the microseismicity during 417 days following the M_W 4.5 earthquake. Being the largest event in this region since the 1999 M_W 7.4 Izmit earthquake and its aftershocks, this represents a rare opportunity to benefit from near-fault monitoring and multi-sensor observations in the region.

Complexity of tectonics and fault slip at the Armutlu peninsula

The Sea of Marmara represents a transitional region between the plate-bounding right-lateral strike-slip tectonics of the North Anatolian Fault Zone (NAFZ) (Barka et al., 1992; Bohnhoff et al., 2016) east of the Marmara region and the north-south extension of western Anatolian driven by the slab pull of the Hellenic subduction zone (e.g. Flerit et al., 2004). In contrast to the well-defined and more narrow fault trace of the NAFZ along most of its onshore portion, the Sea of Marmara represents a large pull-apart structure with elastic and permanent strain distributed along two or more main fault branches (Fig. 1) (e.g. Le Pichon et al., 2001; Meade et al., 2002; Armijo et al., 2005).

The Cinarcik fault branch bounds the Çinarcik basin below the eastern Marmara Sea to the south (Bohnhoff et al., 2013; Malin et al., 2018; Martínez-Garzón et al., 2019). The region also hosted the westernmost tip of the 1999 M 7.4 Izmit earthquake rupture (Armijo et al., 2005). The Cinarcik fault zone may have hosted the M 6.3 normal faulting earthquake in 1963 (Pinar et al., 2003; Bulut & Aktar, 2007), the second-largest earthquake in the Marmara region during the instrumental era (Fig 1). This region has been interpreted as a horsetail splay fault structure associated with a major normal fault (Kinscher et al., 2013). The local deformation is partitioned across a complex network of multiple faults with varying orientations including predominant NE–SW extension with significant vertical displacement (Eisenlohr, 1995; Straub et al., 1997). Field observations and seismic moment tensors of selected earthquakes confirmed previous models interpreting the Armutlu peninsula as a Horst structure in a transtensional active pull-apart environment of the Sea of Marmara region (Kinscher et al., 2013). Stress inversion of focal mechanisms derived a local trend of the maximum compressive stress in the range $Tr_{\sigma_1} = N306°\mathrm{E} - \mathrm{N}328°\mathrm{E}$ (Wollin et al., 2018).

The northern portion of the Armutlu Peninsula hosts one of the highest background seismicity rates in the Sea of Marmara extending down to approximately 12 km depth (Wollin et al., 2018; Martínez-Garzón et al., 2019). Recently, it was found that the region also experiences slow deformation transients based on the observation of a 50-day slow strain transient that started after the occurrence of a M_W 4.2 offshore earthquake on June 25th 2016 near the town of Yalova (Malin et al., 2018; Martínez-Garzón et al., 2019). Assuming the source of the slow slip transient to be the same as that activated by the M_W 4.2 earthquake, this signal represented transient slip equivalent to a M_W 5.7 earthquake (Martínez-Garzón et al., 2019). Unfortunately, the source of the slow slip event could not be resolved due to the lack of available nearby GNSS data at that time and the lack of near-fault stations at the offshore segments of the fault. East of the Armutlu peninsula where post-seismic deformation from the 1999 M_W 7.4 Izmit earthquake is still noticeable after 20 years (Özarpacı et al., 2021), a 1 month lasting shallow slip transient was identified along the Gulf of Izmit on December 2016 using InSAR complemented with GPS data (Aslan et al., 2019) but no connection to seismicity trends was established.

Data and Method

Generation of microseismicity catalog

We developed a seismicity catalog (provided in Martínez-Garzón et al., 2021) for the northern portion of the Armutlu peninsula (purple rectangle in Fig 1a), utilizing continuous waveform recordings from the temporary SMARTnet seismic network (Fig 1b), four permanent GONAF borehole vertical seismic arrays (Bohnhoff et al., 2017), and four seismic stations from the permanent regional KOERI seismic network. The time period analyzed in this study covers 417 days following the December, 20th, 2018 Esenkoy M_W 4.5 earthquake, out of which the SMARTnet network provided data from January 29th, 2019 to February 10th, 2020 (387 days). SMARTnet was composed of five broadband Trillium compact seismometers, ten Mark 1 Hz seismometers and ten HL-6B geophones with natural frequencies of 4.5 Hz. Five additional Mark seismometers were installed from July 2019 onwards.

The processing scheme applied to the waveform recordings is summarized in Fig. S1 in the electronic supplement to this article. First, a classical STA/LTA detector was run on each station (vertical component). Triggered signals were classified as eventual local seismic events if detected at least at five stations within a maximum time window of 4 s. All detections were manually revised and false detections, coherent signals of non-tectonic origin and teleseismic events were removed. About 2,800 seismic events displayed sufficient signal to noise ratio and were selected for further processing.

Next, the P- and S- wave arrivals of seismic events from the first six months of the catalog were manually picked (988 seismic events). The manually picked subset was used to train a picking algorithm based on a convolutional neural network. Subsequently, we picked automatically the arrival of P- and S-waves for the remaining data set. Manual refinement of the automatic picks was performed for all seismic events with $M>2$. A total of 29,275 and 20,306 arrival times of P- and S- waves were obtained, respectively.

Initial absolute hypocentral locations of the events were obtained using HYPOINVERSE (Klein, 2002) and a 1-D local velocity model (Bulut et al., 2009), after correcting for station residuals. In the following, we focus on the northern portion of the Armutlu Peninsula, where the coverage provided by our network is optimal. Within the study region (Lon [28.75° – 29.22°E] Lat [40.52°-40.7°N]), a total of 1,642 seismic events were successfully located within the analyzed time period. Median horizontal and vertical absolute location errors for the manually picked events were 1 km and 0.69 km, respectively, while the same values for the automatically picked events by the convolutional neural network increased to 1.24 km and 0.84 km, respectively.

Moment magnitudes (M_W) of the located microearthquakes were estimated utilizing a spectral fitting approach (e.g. Kwiatek et al., 2011). We fixed the quality factor parameters to $Q_P = 750$ and $Q_S = 350$ in agreement with other source parameters and attenuation studies in the region (Gündüz et al., 1998). We estimated the final moment magnitude of each event as the median of the calculated magnitudes from the different stations using both P- and S- waves, however, estimations using both, only P- or only S- phases are highly consistent (Fig. S2 in the electronic supplement to this article). The magnitudes obtained for these events were in the range M_W [0.7, 3.5] (Fig. S3a in the electronic supplement to this article). We identified 95 common events between our catalog and the catalog from the permanent Turkish national seismic network from AFAD (https://deprem.afad.gov.tr/depremkatalogu?lang=en) within the analyzed region and time frame. Comparing their local magnitudes M_L with our moment magnitudes M_W, we fitted a linear regression obtaining the equation $M_W = 0.6M_L + 1.2$ between the two magnitude scales. Based on the minimum curvature method (Woessner & Wiemer, 2005), a magnitude of completeness $M_W^c = 1.4$ ($M_L^C = 1.2$) was obtained, and a b-value $b = 1.08 \pm 0.03$ from the magnitude-frequency Gutenberg-Richter distribution was obtained for the entire study area (Fig. S3b in the electronic supplement to this article). According to the Gutenberg-Richter relation, a slight deficit in large magnitude events (M_W > 2.5) is noticeable in the catalog.

The relative precision of the hypocenters was further refined by relocating the seismicity utilizing the double-difference approach (Waldhauser & Ellsworth, 2000). A total of 209,106 travel time differences from P- and S- waves catalog arrival times were employed to perform the relocation. In the last iterations, we folded in 8,500 additional travel time differences obtained from P-wave waveform cross-correlation to improve the resolution at the scale of 500 m. A total of 831 seismic events from the study region were successfully relocated. Relative horizontal and vertical relocation precision of 130 m and 40 m were achieved assuming 68% confidence interval, respectively, as estimated from bootstrap resampling. The relocated seismicity catalog together with error ellipses for each event is provided in Fig. S4 in the electronic supplement to this article.

Estimation of double-couple seismic moment tensors

A portion of the dataset displayed a sufficient number of stations available and enough azimuthal coverage to allow for a double-couple seismic moment tensor (MT) inversion. To this end, a total of 4,238 amplitudes of the P-wave first-motion arrival were manually picked from a subset of events with magnitude $M_W \geq 1.5$. We subsequently utilized the arrivals to calculate the double-couple MTs of the corresponding microseismicity. The inversion was performed with the fociMT software (Kwiatek et al., 2016) based on the simultaneous inversion of P-wave polarities and amplitudes. Take-off angles between the hypocenters and each station were calculated utilizing a version of the 1-D velocity model from Bulut et al., (2009), interpolated every km to avoid sharp changes in the ray paths due to events close to the boundary between two velocity layers. A total of 243 MTs were calculated based on recordings at 10 to 25 stations. The epicentral distances between the utilized stations and the seismicity varied from 450 m up to 50 km, with a median value of 11.9 km. The vast majority of recorded phases correspond to direct waves with a median take-off angle of 133°.

Based on the spatial distribution of the events for which MTs could be calculated and the areas of interest, we manually grouped the seismicity into seven different areas. For each of them, ray paths from the hypocenters to the stations were assumed to be similar, and we applied the iterative hybrid technique hybridMT (Kwiatek et al., 2016) to refine the MT solutions and identify potential stations with incorrect sensitivity and/or suffering from strong site effects. A total of 157 MTs could be refined using this technique. For each of the defined MT groups, we estimated their median fault plane variability ϑ to characterize the heterogeneity of the fault plane solutions (e.g. Goebel et al., 2017). This was achieved by calculating the 3-D rotation angle between each pair of focal mechanisms (Kagan, 1991).

We additionally estimated the double-couple MTs of the M_W 4.5 earthquake that occurred south of the Esenkoy village on December, 20th, 2018, and the M_W 4.1 earthquake that occurred on November 30th 2018 in the same region, marking the beginning of the sequence. As these event occurred more than one month before the deployment of the SMARTnet seismic network, we used the amplitudes and polarities from the permanent GONAF stations, as well as publicly available waveform data for this event from the national seismic networks operated by AFAD and KOERI. For these two events, a total of 24 and 28 stations with high quality recordings were finally employed from the entire Sea of Marmara region, respectively, ensuring a complete azimuthal coverage of the focal sphere. Then, the focal mechanism inversion for these events was performed following the methodology described above.

Processing of strainmeter data

The eastern Sea of Marmara region hosts six Gladwin tensor borehole strainmeters at different locations deployed by UNAVCO in wellbores at 150 m depth. A summary of the main features of these strainmeters is provided in Martínez-Garzón et al. (2019). We focus here on the two strainmeters located in the Armutlu Peninsula, near the villages of Esenkoy (GONAF-ESN1) and Armutlu (GONAF-BOZ1) (Fig.1a). These strainmeters are located at epicentral distances of 5.5 km and 22 km from the M_W 4.5 event, respectively.

Processing of the strainmeter recordings is routinely performed by UNAVCO and includes the down-sampling from 1 s to 300 s to simplify data handling. Tidal corrections and borehole trends were generated and applied to the strainmeter recordings following Hodgkinson et al., (2013). Corrections for the M2 and O1 tidal modes are calculated using the SPOTL tidal program and subtracted from each gauge before combination. Borehole trend corrections are calculated by fitting exponential functions to the raw data from the four different gauges of the strain tensor during the entire time of data acquisition. From these corrected data from the four gauges of the Gladwin strainmeters, three strain components were calculated, namely the areal strain ε_{N+E}, differential strain ε_{E-N} and engineering strain $2\varepsilon_{EN}$, defined as:

$$\begin{aligned} \varepsilon_{N+E} &= \varepsilon_{EE} + \varepsilon_{NN} \\ \varepsilon_{E-N} &= \varepsilon_{EE} - \varepsilon_{NN} \\ 2\varepsilon_{EN} &= \varepsilon_{EN} + \varepsilon_{NE} \end{aligned} \qquad [1]$$

where ε_{EE}, ε_{NN} and ε_{EN} represent the three independent components of the horizontal strain tensor and the symmetry condition $\varepsilon_{EN} = \varepsilon_{NE}$ applies.

Results

Episodic seismic sequences located around the M_W 4.5 2018 Esenkoy earthquake source area

A total of 1,041 out of 1,234 events from our catalog with absolute locations and 706 out of 828 events composing the relocated catalog are concentrated in an area south of Esenkoy, forming a number of subparallel aligned structures striking NW-SE (Figs. 1b, 2). Except for a sequence of events occurring in December 2019 (red-colored events in Fig. 2), most of the seismicity delineates a planar fault structure dipping approximately 60° towards North-East, which was activated between 7 and 12 km depth (Fig. 2a). The located seismicity is provided in Martínez-Garzón et al., (2021).

At the northeastern edge of this area (the deepest portion), a M_W 4.1 event occurred in this area on November 30th, 2018 at a depth of 14 km. After 20 days, on December 20th 2018 a M_W 4.5 earthquake occurred (hereafter referred to as the 2018 Esenkoy M_W 4.5 earthquake, Fig. 2) about 2.5 km epicentral distances from the first event. Since this event occurred approximately one month before the deployment of our temporary SMARTNET seismic network, we utilized the AFAD seismicity catalog to check the seismicity preceding and immediately following the M_W 4.5 earthquake. The AFAD catalog contained 106 events from November 30th 2018 to January 29th, 2019, including 36 and 70 events before and after the M_W 4.5 earthquake, respectively. The main shock ruptured the deepest portion of this active fault patch (11 km). The seismicity during the first month following the M_W 4.5 earthquake activated up to the shallowest edge of this active fault plane at about 7 km (Fig 2). Assuming a static stress drop value of $\Delta\sigma = 1MPa$ and a Madariaga source model, a M_W 4.5 earthquake should rupture a circular region with source radius of about $r \approx 1km$ (Kwiatek et al., 2011). The observed seismically activated volume covering 7 km x 7 km x 5 km is therefore significantly larger than the rupture area of the mainshock.

Following the M_W 4.5, the seismicity in this region shows clear spatio-temporal variations. We identified at least four episodic sequences, each of them lasting for few days and containing one or more days with > 30 earthquakes per day (Fig. 3a). The largest number of events in each of the sequences occurred 53, 143, 202 and 338 days after the M_W 4.5 earthquake (Fig. 3a). Within the first of these sequences (dark blue color in Fig. 2) the seismicity covered approximately the central part of the planar structure. The second sequence (turquoise color) propagated towards the edges of the activated area in the first sequence. The third and fourth sequences (light green and red colors in Fig. 2) were more spatially clustered and they only reach 2 km and 4 km away from the M_W 4.5 epicentral location, respectively.

Slow slip transient following the 2018 Esenkoy M_W 4.5 earthquake

The recordings of the BOZ1 and ESN1 strainmeters show a strain transient in the differential (Fig. 3b) and engineering (Fig. 3c) components starting at the origin time of the M_W 4.5 Esenkoy earthquake. The main transient strain signal, which is observed in both strainmeters lasted about 30 days (light blue rectangles in Fig 3). Following a period of about 33 days during which the first seismic sequence occurred, a potential transient of smaller amplitude could be identified during the subsequent 30 days only the BOZ1 strainmeter (light green rectangles in Fig. 3). After the first three months from the M_W 4.5 earthquake, the strain recordings display a slow recovery towards the original strain level before the earthquake, which is reached about 250 days from the occurrence of the event. The recordings of the ESN1 strainmeter, located closer to the M_W 4.5 epicenter, are less clear (Figs. 3b, 3c) and to some extent affected by the overall state of extension of three of the strainmeter gauges during this time period, which decreases the sensitivity of the instrument. The ESN1 time series contain data gaps shortly after the November 30th, 2018 M_W 4.1 earthquake (red dashed line in Fig. 3) and right after the December 20th 2018 M_W 4.5 earthquake. Furthermore, the ESN1 recordings display a number of spikes that are likely electronic noise signals introduced by the power net. We find that the temporal evolution of differential and engineering components at ESN1 follow overall a similar trend and shape as at BOZ1. Neither of the areal components -being more sensitive to vertical strain changes- of BOZ1 or ESN1 indicate a large change at this time (see Fig. S5 in the electronic supplement to this article including a longer time period of strainmeter recordings). This suggests that the observed transient is likely not related to atmospheric variations. The next closest strainmeter, SIV1 (Fig. 1), did not record during the main months analyzed here. The other regional strainmeters are all >35 km away and displayed no clear changes that can be associated with the occurrence of the M_W 4.5 Esenkoy earthquake.

To estimate the source location of the observed strain transient, we use an Okada dislocation model (Okada, 1985) and calculated the deformation fields from fault sources at various locations and with different fault parameters. We tested the configurations that best match the sign of the recordings from the differential, engineering and areal strain components of the two available strainmeters. Three different scenarios were tested, where the slow slip source was placed (a) on the local seismogenic plane activated during this sequence (Fig. 2), (b) along a potential onshore segment of the Cinarcik Fault between the BOZ1 and ESN1 strainmeters, and (c) on the onshore segment of the Cinarcik Fault where a M > 4 earthquake occurred in 2008. For each of these scenarios, between 30 and 60 models were run with varying strike, dip, rake and hypocentral depth parameters according to the geometry of the fault sources (Table S1 in the electronic supplement to this article). The best fitting model could reproduce five out of the six observations, and it was obtained centering the fault at the epicentral location of the M_W 4.5 earthquake (scenario a) and the following geometrical parameters $\varphi = 305, \delta = 55,\ \lambda = -110$, $z = 3\ km$ and M_W = 5 (Fig. S7 in the electronic supplement to this article). Therefore, we suggest that the slow slip transient activated the shallower portion of the fault plane that hosted the M_W 4.5 event and subsequent three sequences.

Repeated activation of the M_W4.5 mainshock rupture and a nearby fault

We classified the 243 MTs according to their Andersonian faulting style (i.e. normal faulting, strike-slip or reverse) depending on which of the P, T or B axes is closer to vertical. 138 MTs (57% of the total) indicated normal faulting events, 91 (37% of the total) displayed strike-slip faulting, and a minority of 14 thrust events (6% of the total) were obtained. From the region analyzed here, 106 MTs were available for further analysis.

The 2018 M_W 4.5 Esenkoy earthquake ruptured with normal faulting kinematics. Strike, dip and rake values of $\varphi = 309°, \delta = 55°, \lambda = -110°$ were obtained, respectively (Fig 4). These values are in good agreement with the geometry of the planar structure defined by the microseismicity (Fig 2b). The previous M_W 4.1 event on November 30th, 2018 displayed a very similar focal mechanism, with $= 300°, \delta = 64°, \lambda = -122°$, likely indicating that the same fault structure ruptured the two events (Fig 2b). In the following, we analyze the moment tensors within the four different high-seismicity areas using the hybridMT inversion (see Fig 4a for the regions enclosed in each group). Group A comprises the region around the M_W 4.5 2018 Esenkoy event and roughly corresponds to sequence 3, occurring around July 10th 2019 (light green colors in Fig 2). The 40 estimated moment tensors included 33 normal faulting and 7 strike-slip events. The moment tensors are highly consistent with both the M_W 4.5 earthquake and the planar structure defined by the hypocenters (Fig 4). Group A shows the lowest fault plane variability compared to groups B-C, with a median 3D rotation angle between focal mechanisms $\vartheta_A = 26°$. Groups B and C contain 17 and 19 events, respectively, and they correspond to the southern portion of the planar fault structure. The average MT as well as 27 individual solutions represent normal faulting, similar to those from Group A and the M_W 4.5 event (Fig 4). However, the median fault plane variabilities are larger ($\vartheta_B = 74°$ and $\vartheta_C = 56°$), reflecting larger fault plane heterogeneity. Group D contains 30 MTs and corresponds to the fourth sequence (red circles in Fig. 2, around November 24th , 2019) where the seismicity occurred in a separate patch of about 2 x 2 km^2 off the fault plane defined by the seismicity of the other sequences (Fig 2). In this case, a majority of pure strike-slip faulting events are obtained, with a strike-slip average moment tensor and very low median fault plane variability of $\vartheta_1 = 22°$. The different MT and seismicity distribution suggest that the fourth sequence likely activated a separate fault structure with different orientation and kinematics. Here, the seismicity does not form a first-order planar structure. However, the nodal plane that seem to best fit the seismicity has fault parameters, $\phi = 189°, \delta = 60°, \lambda = 5°$, thus representing a left-lateral strike-slip fault.

Seismicity migration patterns

We investigated the migration patterns of the seismicity away from the M_W 4.5 event by projecting the hypocenters of the first three sequences onto the main fault on the best-fitting plane. Then, we calculated the in-plane distance between the 2018 M_W 4.5 hypocenter and each earthquake as a function of time (Fig. 5). We included the seismicity from AFAD catalog for the times between the occurrence of the M_W 4.1 event on Nov 30th, 2018 and the beginning of the SMARTnet catalog. The temporal pattern during the first month of seismicity around the M_W 4.5 earthquake can be fitted with an Omori's Law of the form $N(t) = {}^{k}/_{t^p}$, where $k = 206$ and $p = 1.3$ (Fig. S8 in the electronic supplement to this article). Focusing on the propagation of seismicity away from the M_W 4.5 mainshock during the first month after its occurrence, we found that the in-plane distance of events to the mainshock initially grows with log time (Fig. 5b, 5c). The logarithmic behavior of the seismicity migration suggests the rupture of several asperities being loaded by afterslip driven by brittle creep after the M_W 4.5 event (e.g. Perfettini et al., 2018).

After the first month of typical aftershock decay, the seismicity rates increased again departing from the Omori law. The temporal evolution of the seismicity from the studied region revealed four distinct sequences (cf. Fig. 3). While the duration of the four sequences is comparable, including one to three days with >30 events per day (Fig. 3a), the magnitude distribution (Fig. 5a) and activated volumes differ between sequences. The first and second sequences contained no earthquake with $M_W > 2.9$, and cannot be well described with a mainshock-aftershock type of occurrence as the larger seismicity rates did not occur at the beginning of the sequence (Fig. 5a) , thus displaying a more swarm-like behavior typical of sequences driven by aseismic slip and/or fluids (e.g. Zaliapin & Ben-Zion, 2013). The events contained in these sequences activated most of the volume surrounding the mainshock up to an epicentral distance of 6 km. The time between the mainshock and sequence 1 and between sequences 1 and 2 is about 50 and 90 days, respectively, thus being comparable. In contrast, sequences 3 and 4 contain one or more events with larger magnitudes ($M_W > 3$) at the beginning of the sequence (Fig. 5a) and these larger events triggered productive aftershock sequences tightly clustered in space.

Discussion

Mechanisms driving the episodic seismic activity in the 2018 M_W 4.5 Esenkoy earthquake region

The occurrence of seismic sequences following a mainshock around its rupture area and beyond may be explained by several physical mechanisms. Coseismic static or dynamic stress changes will perturb the stress distribution in the region surrounding the mainshock area (e.g. King et al., 1994; Stein et al., 1997). Also, pore-pressure diffusion along pre-existing or fresh fractures in the mainshock-perturbed area can promote the occurrence of aftershocks (e.g. Miller et al., 2004). Seismicity driven by fluid migration should roughly follow a diffusion equation (Shapiro et al., 2003):

$$r = \sqrt{4\pi D t}, \qquad [2]$$

where r is the distance from a reference point and D represents the diffusivity coefficient that may take a range of values from $0.25\,{}^{\mathrm{m}^2}/_{\mathrm{s}}$ to $200\,{}^{\mathrm{m}^2}/_{\mathrm{s}}$ (Shapiro et al., 2003). Seismic sequences driven by migration of fluids have been observed for example near the Salton Trough (Chen & Shearer, 2011) or in the Long Valley Caldera (Shelly et al., 2016), both located in California. Seismic sequences may also be driven by aseismic slip, either as afterslip accommodated by brittle creep (Perfettini & Avouac, 2004) or by slow slip transients releasing accumulated tectonic stresses (e.g. Taira et al., 2014). Aftershock migration driven by afterslip follows a logarithmic dependence of the form (Perfettini et al., 2018):

$$r \propto Alog(t). \qquad [3]$$

Combination of one or more of these processes is also possible. For example, afterslip and fluid diffusion were proposed to explain the temporal evolution of the aftershocks of the M_W 7.2 2010 El Mayor-Cucapah earthquake (Ross et al., 2017).

The normal fault that ruptured in the 2018 M_W 4.5 Esenkoy earthquake and off-fault structures remained active during at least the following 250 days, in three different seismicity sequences. The Armutlu Peninsula is a fluid rich environment and it hosts several hot springs and geothermal activities (Eisenlohr, 1995). However, it is not clear whether any of the sequences follow the pattern of a fluid pressure diffusion front with typical diffusivity values comparable to other case studies (see for example red line in Figs. 5b, 5c for $D = 0.6\,{}^{m^2}/_{s}$). This indicates that the episodic seismic activity is likely not due to just pore pressure diffusion. Instead, our observations may be best explained by the rupture of asperities being loaded by aseismic slip at least during the first two sequences, including: (1) the observation of a transient signal at two strainmeters in the 30 days following the occurrence of the M_W 4.5 Esenkoy earthquake before Sequence 1 (Fig. 3) (2) the migration of the seismicity from the mainshock followed a logarithmic relation in time (particularly during the first month), as previously observed for afterslip, (3) comparable time intervals between the different sequences, suggesting continuous loading from some aseismic or slow source and (4) the lack of a clear mainshock-aftershock sequence within sequences 1 and 2 compared to sequences 3 and 4, resembling swarm-like clustering, which has been related in some case to the occurrence of aseismic slip (e.g. Chen and Shearer, 2011; Ross et al., 2017). After the occurrence of the first two seismic sequences, stress redistribution around the mainshock area likely caused breaking of remaining asperities in the vicinity. This hypothesis is supported by the larger events contained in sequences 3 and 4 (with $M_W > 3$) (Fig. 5a), the smaller epicentral distances between the M_W 4.5 earthquake and these sequences (Fig. 5b) and the clustering of events from sequences 3 and 4 around their own mainshock (Fig. 5b). This suggests breaking of a single asperity in each of these sequences rather than the activation of a larger fault segment driven by aseismic slip.

The proposed activation of asperities due to slow slip partly depends on the temporal continuity of the magnitude of completeness and the consistence of epicentral location quality between the SMARTnet and AFAD catalogs that were used throughout this study. We therefore tested whether the inference of episodic seismicity after the M_W 4.5 earthquake may be affected by the lower M_C during operation of the SMARTnet network. For that purpose, we checked seismicity rates every two days observed from January 2016 until 417 days after the occurrence of the M_W 4.5 earthquake using the AFAD catalog (Fig S6 in the electronic supplement to this article). The seismic activity following the M_W 4.5 earthquake is enhanced in comparison to the activity observed before the event. In addition, seismicity rates for sequences 1, 3, and 4 clearly exceed any potential seismic activity fluctuations observed before the mainshock using the AFAD catalog, except for a seismicity cluster in September 2016 which could be linked to the occurrence of a previously reported slow slip transient (Martínez-Garzón et al., 2019; Durand el at., in prep). Finally, we tested whether the epicentral location uncertainty of the M_W 4.5

event influences the suggested seismicity migration pattern. The observed seismicity migration pattern does not depend on the selected M_W 4.5 epicentral location (within its uncertainties).

Afterslip v triggered slow slip in the eastern Marmara region

While earthquake afterslip relieves coseismic stress increases from recent earthquake ruptures, triggered slow slip transients release preexisting tectonic stress and they could be triggered by both static and dynamic stresses (Burgmann, 2018). As the timescale of relaxation depends on the initial stress perturbation, the duration of resolvable afterslip is dependent on the mainshock magnitude (Wang et al., 2012). Accordingly, afterslip has been reported to cover different time scales, ranging from few days after M < 5 earthquakes (e.g. Hawthorne et al., 2016 for moderate events on the San Andreas Fault) up to 200 days after the occurrence of the M_W 7.6 Chi-Chi earthquake (Perfettini & Avouac, 2004). Seismicity driven by afterslip is observed to decay following Omori law and it is expected to propagate logarithmically from the mainshock. This is in good agreement with our observations of the seismicity during the first month after the M_W 4.5 earthquake. However, the duration of the subsequent slow slip appears unusually long with respect to the mainshock magnitude. Differently from afterslip, the duration of triggered slow slip transients is expected to be independent of the triggering mainshock (e.g. Taira et al., 2014). Therefore, it is possible that the stress changes from the M_W 4.5 Esenkoy earthquake and its following afterslip may have triggered a transient slow slip event, which would explain the relatively large duration and strain values of the aseismic transients observed here. These two types of processes can be difficult to separate, as regions displaying large earthquake afterslip duration and amplitude also tend to experience slow slip transients during the interseismic cycle (Rolandone et al., 2018).

The here reported case is the second observation of combined long-lasting afterslip and the triggering of a slow strain transient after M4+ earthquakes in the region. In 2016, a slow-slip transient lasting about 50 days was identified after the occurrence of a M_W 4.2 offshore earthquake in the Çinarcik basin (Martínez-Garzón et al., 2019). The identification of two slow transients within a time span of a few years suggests that aseismic deformation in the eastern Sea of Marmara may contribute to fault slip more than previously expected. Many questions still remain open, such as the depth extent of the source of these slow signals. Therefore, the postseismic behavior of moderate earthquakes (occurring more often than larger hazard-prone events) needs to be monitored by near-fault instrumentation and analyzed in greater detail to evaluate how frequent strong postseismic transients are in the eastern Sea of Marmara region and elsewhere.

Concluding remarks

Identifying and quantifying interaction between seismic and aseismic deformation is essential to better understand loading and unloading of distinct fault segments, which, in turn, is of critical importance for improved quantitative hazard and risk assessment in the Marmara region given the proximity to the Istanbul metropolitan region. We combined microseismicity analysis from a new temporary seismic network (SMARTnet) and borehole strainmeter data to resolve the mechanisms driving the persistent seismic activity around the 2018, Dec 20th M_W 4.5 earthquake, onshore the Armutlu peninsula of the Sea of Marmara region during the following 417 days. The bulk of the recorded seismicity corresponds to three sequences occurring every 50-90 days with > 30 events per day. It ruptured a local normal fault structure within and beyond the rupture area of a M_W 4.5 event. A fourth sequence ruptured a nearby strike-slip structure. The migration of the seismicity from the M_W 4.5 earthquake followed a logarithmic fit. The migration patterns, the periodicity of the activated seismicity bursts, the swarm-like behavior of the seismicity during the first two sequences, and an observed slow slip signal in two strainmeters suggests that at least the first two seismic sequences may have been primarily driven by aseismic slip potentially combined with fluid migration along the fault. Finally, we posit that a local strain transient has been triggered by the M_W 4.5 event and its afterslip.

Data and Resources

Seismograms and earthquake catalog from this network have been acquired with the SMARTnet, GONAF and KOERI seismic networks. Earthquake catalog is available online through the GFZ Data Services in Martínez-Garzón et al., (2021). Data from the strainmeters is based on services provided by the GAGE Facility, operated by UNAVCO, Inc., with support from the National Science Foundation and the National Aeronautics and Space Administration under NSF Cooperative Agreement EAR-1724794. Seismic catalog from AFAD is available at https://tdvms.afad.gov.tr/ (last accessed 13.01.2021). Continuous recordings from the utilized KOERI stations are available at: (http://www.koeri.boun.edu.tr/sismo/2/earthquake-catalog/, last accessed on 28/01/2021). Strain modelling has been performed using the core from Coulomb 3.3 software (https://www.usgs.gov/software/coulomb-3, last accessed on 15.05.2021). Supplemental Material for this article includes eight figures (Fig S1 to S8) and a table (Table S1).

Acknowledgements

The installation and maintenance of a network would not have been possible without the help of many persons. We would like to particularly thank Digdem Acarel for her important help assisting maintenance during Covid-19 times, Mustafa Poyraz, Selim Sezer and Müdürnü Aziz Aksoy from AFAD for their help with the logistics of the network and finding optimal locations, and Claudius Marx, Amandine Amemoutou, Maria Leonhard and Christopher Wollin for their help with the network maintenance. We would like to specially thank Dave Mencin and Kathleen Hodgkinson from UNAVCO for fruitful discussions about the transients observed in the strainmeter data. We thank the Editor Allison Bent, an Associate Editor, Roland Burgmann and an anonymous reviewer for constructive editing and reviews that greatly improved the paper. P.M.G., V.D. and S.B. acknowledge funding from the Helmholtz Association in the frame of the Young Investigators Group VH-NG-1232 (SAIDAN). Seismic instruments of the SMARTnet network were provided by Geophysical Instrument Pool Potsdam (GIPP) of the GFZ, grant numbers GIPP201819 and GIPP201921.

References

Armijo, R., Pondard, N., Meyer, B., Uçarkus, G., de Lépinay, B. M., Malavieille, J., et al. (2005). Submarine fault scarps in the Sea of Marmara pull-apart (North Anatolian Fault): Implications for seismic hazard in Istanbul. *Geochemistry, Geophysics, Geosystems, 6*(6), Q06009. https://doi.org/10.1029/2004GC000896

Aslan, G., Lasserre, C., Cakir, Z., Ergintav, S., Özarpaci, S., Dogan, U., et al. (2019). Shallow Creep Along the 1999 Izmit Earthquake Rupture (Turkey) From GPS and High Temporal Resolution Interferometric Synthetic Aperture Radar Data (2011–2017). *Journal of Geophysical Research: Solid Earth, 124*(2), 2218–2236. https://doi.org/10.1029/2018JB017022

Barka, A. A. (1992). The North Anatolian fault zone. *Annales Tectonicae, Spec. Iss., VI*, 164–195.

A. Barka, H. S. Akyu¨z, E. Altunel, G. Sunal, Z. C¸ akir, A. Dikbas, B. Yerli, R. Armijo, B. Meyer, J. B. de Chabalier, T. Rockwell, J. R. Dolan, R. Hartleb, T. Dawson, S. Christofferson, A. Tucker, T. Fumal, R. Langridge, H. Stenner, W. Lettis, J. Bachhuber, and W. Page. The Surface Rupture and Slip Distribution of the 17 August 1999 I˙zmit Earthquake (M 7.4), North Anatolian Fault Bulletin of the Seismological Society of America, 92, 1, pp. 43–60, February 2002

Bedford, J., Moreno, M., Baez, J. C., Lange, D., Tilmann, F., Rosenau, M., et al. (2013). A high-resolution, time-variable afterslip model for the 2010 Maule Mw = 8.8, Chile megathrust earthquake. *Earth and Planetary Science Letters, 383*, 26–36. https://doi.org/10.1016/j.epsl.2013.09.020

Bohnhoff, M., Dresen, G., Ceken, U., Kadirioglu, F. T., Kartal, R. F., Kilic, T., et al. (2017). GONAF-the borehole Geophysical Observatory at the North Anatolian Fault in the eastern Sea of Marmara. *Scientific Drilling, 5,* 1–10.

Bohnhoff, Marco, Martínez-Garzón, P., Bulut, F., Stierle, E., & Ben-Zion, Y. (2016). Maximum earthquake magnitudes along different sections of the North Anatolian fault zone. *Tectonophysics*, *674*, 147–165. https://doi.org/10.1016/j.tecto.2016.02.028

Bohnhoff, Marco, Grosser, H., & Dresen, G. (2006). Strain partitioning and stress rotation at the North Anatolian fault zone from aftershock focal mechanisms of the 1999 Izmit Mw= 7.4 earthquake. *Geophysical Journal International*, *166*(1), 373–385. https://doi.org/10.1111/j.1365-246X.2006.03027.x

Bulut, F., & Aktar, M. (2007). Accurate relocation of İzmit earthquake (Mw = 7.4, 1999) aftershocks in Çınarcık Basin using double difference method. *Geophysical Research Letters*, *34*(10), n/a-n/a. https://doi.org/10.1029/2007GL029611

Bulut, F., Bohnhoff, M., Ellsworth, W. L., Aktar, M., & Dresen, G. (2009). Microseismicity at the North Anatolian Fault in the Sea of Marmara offshore Istanbul, NW Turkey. *Journal of Geophysical Research: Solid Earth*, *114*(B9), B09302. https://doi.org/10.1029/2008JB006244

Bürgmann, R. (2018). The geophysics, geology and mechanics of slow fault slip. *Earth and Planetary Science Letters*, *495*, 112–134. https://doi.org/10.1016/j.epsl.2018.04.062

Chen, X., & Shearer, P. M. (2011). Comprehensive analysis of earthquake source spectra and swarms in the Salton Trough, California. *Journal of Geophysical Research: Solid Earth*, *116*(B9), B09309. https://doi.org/10.1029/2011JB008263

Dresen, G., Kwiatek, G., Goebel, T., & Ben-Zion, Y. (2020). Seismic and Aseismic Preparatory Processes Before Large Stick–Slip Failure. *Pure and Applied Geophysics*, *177*(12), 5741–5760. https://doi.org/10.1007/s00024-020-02605-x

Eisenlohr, T. (1995). Die Thermalwasser der Armutlu-Halbinsel (NW-Turkei) und deren Beziehung zu Geologie und aktiver Tektonik. ETH Zurich (PhD Thesis).

Flerit, F., Armijo, R., King, G., & Meyer, B. (2004). The mechanical interaction between the propagating North Anatolian Fault and the back-arc extension in the Aegean. *Earth and Planetary Science Letters*, *224*(3–4), 347–362. https://doi.org/10.1016/j.epsl.2004.05.028

Goebel, T. H. W., G. Kwiatek, T. W. Becker, E. E. Brodsky, and G. Dresen (2017). What allows seismic events to grow big?: Insights from b-value and fault roughness analysis in laboratory stick-slip experiments. *Geology* **45,** 815–818, doi 10.1130/G39147.1

Gündüz, H., Ayşe, K.-Ö., Aysun, B.-G., & Niyazi, T. (1998). S-wave attenuation in the Marmara Region, northwestern Turkey. *Geophysical Research Letters*, *25*(14), 2733–2736. https://doi.org/10.1029/98GL02042

Hawthorne, J. C., Simons, M., & Ampuero, J.-P. (2016). Estimates of aseismic slip associated with small earthquakes near San Juan Bautista, CA. *Journal of Geophysical Research: Solid Earth*, *121*(11), 2016JB013120. https://doi.org/10.1002/2016JB013120

Hodgkinson, K., Langbein, J., Henderson, B., Mencin, D., & Borsa, A. (2013). Tidal calibration of plate boundary observatory borehole strainmeters. *Journal of Geophysical Research: Solid Earth*, *118*(1), 447–458. https://doi.org/10.1029/2012JB009651

Inbal, A., Ampuero, J.-P., & Avouac, J.-P. (2017). Locally and remotely triggered aseismic slip on the central San Jacinto Fault near Anza, CA, from joint inversion of seismicity and strainmeter data. *Journal of Geophysical Research: Solid Earth*, 2016JB013499. https://doi.org/10.1002/2016JB013499

Kagan, Y. Y. (1991). 3-D rotation of double-couple earthquake sources. *Geophys. J. Int.*, *106*, 709–716.

King, G. C. P., Stein, R. S., & Lin, J. (1994). Static stress changes and the triggering of earthquakes. *Bulletin of the Seismological Society of America*, *84*(3), 935–953.

Kinscher, J., Krüger, F., Woith, H., Lühr, B. G., Hintersberger, E., Irmak, T. S., & Baris, S. (2013). Seismotectonics of the Armutlu peninsula (Marmara Sea, NW Turkey) from geological field observation and regional moment tensor inversion. *Tectonophysics*, *608*, 980–995. https://doi.org/10.1016/j.tecto.2013.07.016

Klein, F. (2002). User's guide to HYPOINVERSE-2000, a Fortran Program to Solve for Earthquake Locations and Magnitudes. *Open File Report*. Retrieved from NCEDC, http://www.ncedc.org/ftp/pub/doc/ ncsn/shadow2000.pdf

Korkusuz Öztürk, Y., Meral Özel, N., & Özbakir, A. D. (2015). States of local stresses in the Sea of Marmara through the analysis of large numbers of small earthquakes. *Tectonophysics*, *665*, 37–57. https://doi.org/10.1016/j.tecto.2015.09.027

Kwiatek, G., Plenkers, K., Dresen, G., & JAGUARS Research Group. (2011). Source Parameters of Picoseismicity Recorded at Mponeng Deep Gold Mine, South Africa: Implications for Scaling Relations. *Bulletin of the Seismological Society of America*, *101*(6), 2592–2608. https://doi.org/10.1785/0120110094

Kwiatek, Grzegorz, Martínez-Garzón, P., & Bohnhoff, M. (2016). HybridMT: A MATLAB/Shell Environment Package for Seismic Moment Tensor Inversion and Refinement. *Seismological Research Letters*. https://doi.org/10.1785/0220150251

Le Pichon, X., Şengör, A. M. C., Demirbağ, E., Rangin, C., İmren, C., Armijo, R., et al. (2001). The active Main Marmara Fault. *Earth and Planetary Science Letters*, *192*(4), 595–616. https://doi.org/10.1016/S0012-821X(01)00449-6

Malin, P. E., Bohnhoff, M., Blümle, F., Dresen, G., Martínez-Garzón, P., Nurlu, M., et al. (2018). Microearthquakes preceding a M4.2 Earthquake Offshore Istanbul. *Scientific Reports*, *8*(1), 16176. https://doi.org/10.1038/s41598-018-34563-9

Martínez-Garzón, P., Ben-Zion, Y., Zaliapin, I., & Bohnhoff, M. (2019). Seismic clustering in the Sea of Marmara: Implications for monitoring earthquake processes. *Tectonophysics*, *768*, 228176. https://doi.org/10.1016/j.tecto.2019.228176

Martínez-Garzón, P., Bohnhoff, M., Mencin, D., Kwiatek, G., Dresen, G., Hodgkinson, K., et al. (2019). Slow strain release along the eastern Marmara region offshore Istanbul in conjunction with enhanced local seismic moment release. *Earth and Planetary Science Letters*, *510*, 209–218. https://doi.org/10.1016/j.epsl.2019.01.001

Martínez-Garzón, P., Durand, V., Kwiatek, G., Bohnhoff, M., Dresen, G., Turkmen, T. and Nurlu, M. (2021): Seismicity catalog for the Armutlu Peninsula from 2019 derived using the SMARTnet temporary seismic network. V. 1. GFZ Data Services. https://doi.org/10.5880/GFZ.4.2.2021.004

Mavrommatis, A. P., Segall, P., & Johnson, K. M. (2014). A decadal-scale deformation transient prior to the 2011 Mw 9.0 Tohoku-oki earthquake. *Geophysical Research Letters*, *41*(13), 4486–4494. https://doi.org/10.1002/2014GL060139

Meade, B. J., Hager, B. H., McClusky, S. C., Reilinger, R. E., Ergintav, S., Lenk, O., et al. (2002). Estimates of Seismic Potential in the Marmara Sea Region from Block Models of

Secular Deformation Constrained by Global Positioning System Measurements. *Bulletin of the Seismological Society of America*, *92*(1), 208–215. https://doi.org/10.1785/0120000837

Miller, S. A., Collettini, C., Chiaraluce, L., Cocco, M., Barchi, M., & Kaus, B. J. P. (2004). Aftershocks driven by a high-pressure CO2 source at depth. *Nature*, *427*(6976), 724–727. https://doi.org/10.1038/nature02251

Murru, M., Akinci, A., Falcone, G., Pucci, S., Console, R., & Parsons, T. (2016). M ≥ 7 earthquake rupture forecast and time-dependent probability for the sea of Marmara region, Turkey. *Journal of Geophysical Research: Solid Earth*, 2015JB012595. https://doi.org/10.1002/2015JB012595

Okada, Y. (1985). Surface deformation due to shear and tensile faults in a half-space. *Bulletin of the Seismological Society of America*, *75*(4), 1135–1154.

Parsons, T. (2004). Recalculated probability of M ≥ 7 earthquakes beneath the Sea of Marmara, Turkey. *Journal of Geophysical Research: Solid Earth*, *109*(B5), B05304. https://doi.org/10.1029/2003JB002667

Peng, Z., & Gomberg, J. (2010). An integrated perspective of the continuum between earthquakes and slow-slip phenomena. *Nature Geoscience*, *3*(9), 599–607. https://doi.org/10.1038/ngeo940

Perfettini, H., & Avouac, J.-P. (2004). Postseismic relaxation driven by brittle creep: A possible mechanism to reconcile geodetic measurements and the decay rate of aftershocks, application to the Chi-Chi earthquake, Taiwan. *Journal of Geophysical Research: Solid Earth*, *109*(B2). https://doi.org/10.1029/2003JB002488

Perfettini, H., Frank, W. B., Marsan, D., & Bouchon, M. (2018). A Model of Aftershock Migration Driven by Afterslip. *Geophysical Research Letters*, *45*(5), 2283–2293. https://doi.org/10.1002/2017GL076287

Pinar, A., Kuge, K., & Honkura, Y. (2003). Moment tensor inversion of recent small to moderate sized earthquakes: implications for seismic hazard and active tectonics beneath the Sea of Marmara. *Geophysical Journal International*, *153*(1), 133–145. https://doi.org/10.1046/j.1365-246X.2003.01897.x

Pollitz, F. F., Wicks, C. W., & Svarc, J. L. (2021). Coseismic Fault Slip and Afterslip Associated with the 18 March 2020 M 5.7 Magna, Utah, Earthquake. *Seismological Research Letters*. https://doi.org/10.1785/0220200312

Rolandone, F., Nocquet, J.-M., Mothes, P. A., Jarrin, P., Vallée, M., Cubas, N., et al. (2018). Areas prone to slow slip events impede earthquake rupture propagation and promote afterslip. *Science Advances*, *4*(1), eaao6596. https://doi.org/10.1126/sciadv.aao6596

Ross, Z. E., Rollins, C., Cochran, E. S., Hauksson, E., Avouac, J.-P., & Ben-Zion, Y. (2017). Aftershocks driven by afterslip and fluid pressure sweeping through a fault-fracture mesh. *Geophysical Research Letters*, *44*(16), 8260–8267. https://doi.org/10.1002/2017GL074634

Shapiro, S. A., Patzig, R., Rothert, E., & Rindschwentner, J. (2003). Triggering of Seismicity by Pore-pressure Perturbations: Permeability-related Signatures of the Phenomenon. *Pure and Applied Geophysics*, *160*(5–6), 1051–1066. https://doi.org/10.1007/PL00012560

Shelly, D. R., Ellsworth, W. L., & Hill, D. P. (2016). Fluid-faulting evolution in high definition: Connecting fault structure and frequency-magnitude variations during the 2014 Long Valley Caldera, California, earthquake swarm. *Journal of Geophysical Research: Solid Earth*, *121*(3), 2015JB012719. https://doi.org/10.1002/2015JB012719

Stein, R. S., Barka, A. A., & Dieterich, J. H. (1997). Progressive failure on the North Anatolian fault since 1939 by earthquake stress triggering. *Geophysical Journal International*, *128*(3), 594–604. https://doi.org/10.1111/j.1365-246X.1997.tb05321.x

Straub, C., Kahle, H.-G., & Schindler, C. (1997). GPS and geologic estimates of the tectonic activity in the Marmara Sea region, NW Anatolia. *Journal of Geophysical Research: Solid Earth*, *102*(B12), 27587–27601. https://doi.org/10.1029/97JB02563

Taira, T., Bürgmann, R., Nadeau, R. M., & Dreger, D. S. (2014). Variability of fault slip behavior along the San Andreas Fault in the San Juan Bautista Region. *Journal of Geophysical Research: Solid Earth*, *119*(12), 8827–8844. https://doi.org/10.1002/2014JB011427

Tape, C., Holtkamp, S., Silwal, V., Hawthorne, J., Kaneko, Y., Ampuero, J. P., et al. (2018). Earthquake nucleation and fault slip complexity in the lower crust of central Alaska. *Nature Geoscience*, *11*(7), 536–541. https://doi.org/10.1038/s41561-018-0144-2

Taymaz, T., Jackson, J., & McKenzie, D. (1991). Active tectonics of the north and central Aegean Sea. *Geophysical Journal International*, *106*(2), 433–490. https://doi.org/10.1111/j.1365-246x.1991.tb03906.x

Waldhauser, F., & Ellsworth, W. L. (2000). A Double-Difference Earthquake Location Algorithm: Method and Application to the Northern Hayward Fault, California. *Bulletin of the Seismological Society of America*, *90*(6), 1353–1368. https://doi.org/10.1785/0120000006

Wang, K., Hu, Y., & He, J. (2012). Deformation cycles of subduction earthquakes in a viscoelastic Earth. *Nature*, *484*(7394), 327–332. https://doi.org/10.1038/nature11032

Woessner, J., & Wiemer, S. (2005). Assessing the Quality of Earthquake Catalogues: Estimating the Magnitude of Completeness and Its Uncertainty. *Bulletin of the Seismological Society of America*, *95*(2), 684–698. https://doi.org/10.1785/0120040007

Wollin, C., Bohnhoff, M., Martínez-Garzón, P., Küperkoch, L., & Raub, C. (2018). A unified earthquake catalogue for the Sea of Marmara Region, Turkey, based on automatized phase picking and travel-time inversion: seismotectonic implications. *Tectonophysics*. https://doi.org/10.1016/j.tecto.2018.05.020

Wollin, C., Bohnhoff, M., Vavryčuk, V., & Martínez-Garzón, P. (2018). Stress Inversion of Regional Seismicity in the Sea of Marmara Region, Turkey. *Pure and Applied Geophysics*. https://doi.org/10.1007/s00024-018-1971-1

Zaliapin, I., & Ben-Zion, Y. (2013). Earthquake clusters in southern California II: Classification and relation to physical properties of the crust. *Journal of Geophysical Research: Solid Earth*, *118*(6), 2865–2877. https://doi.org/10.1002/jgrb.50178

Mailing Addresses

Patricia Martínez-Garzón, patricia@gfz-potsdam.de

Helmholtz Centre Potsdam, GFZ German Research Centre for Geosciences, Section 4.2: Geomechanics and Scientific Drilling, Telegrafenberg, 14473 Potsdam, Brandenburg, Germany

Virginie Durand, vdurand@gfz-potsdam.de

Helmholtz Centre Potsdam, GFZ German Research Centre for Geosciences, Section 4.2: Geomechanics and Scientific Drilling, Telegrafenberg, 14473 Potsdam, Brandenburg, Germany

Stephan Bentz, bentz@gfz-potsdam.de

Helmholtz Centre Potsdam, GFZ German Research Centre for Geosciences, Section 4.2: Geomechanics and Scientific Drilling, Telegrafenberg, 14473 Potsdam, Brandenburg, Germany

Grzegorz Kwiatek, kwiatek@gfz-potsdam.de

Helmholtz Centre Potsdam, GFZ German Research Centre for Geosciences, Section 4.2: Geomechanics and Scientific Drilling, Telegrafenberg, 14473 Potsdam, Brandenburg, Germany

Georg Dresen, dre@gfz-potsdam.de

Helmholtz Centre Potsdam, GFZ German Research Centre for Geosciences, Section 4.2: Geomechanics and Scientific Drilling, Telegrafenberg, 14473 Potsdam, Brandenburg, Germany

Taylan Turkmen, Taylan.Turkmen@afad.gov.tr

AFAD Yalova Disaster and Emergency Management Authority Turkey, Yalova, Turkey.

Murat Nurlu, murat.nurlu@afad.gov.tr

AFAD Yalova Disaster and Emergency Management Authority Turkey, Ankara, Turkey.

Marco Bohnhoff bohnhoff@gfz-potsdam.de

Helmholtz Centre Potsdam, GFZ German Research Centre for Geosciences, Section 4.2: Geomechanics and Scientific Drilling, Telegrafenberg, 14473 Potsdam, Brandenburg, Germany

Figures

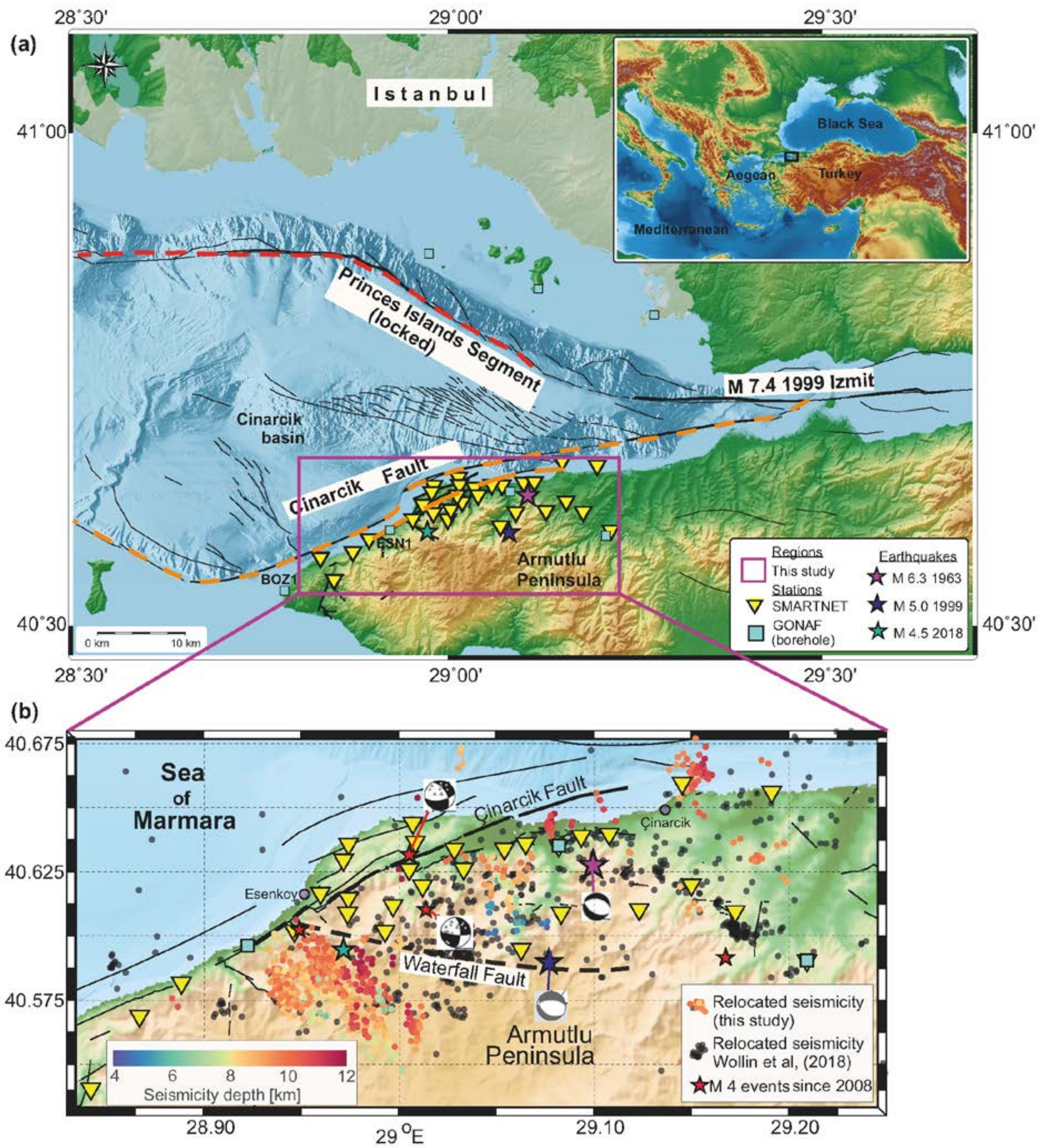

Figure 1: (a) Eastern Sea of Marmara region with the main fault branches of the northern NAFZ strand. The red thick dashed line marks the Princes Islands Segment that is likely locked (Bohnhoff et al., 2013). The black thick line represents the westernmost portion of the 1999 M_W 7.4 Izmit earthquake. The thick dashed orange lines represent the Çinarcik Fault. The purple rectangle marks the study area which is enlarged in (b). (b) Relocated seismicity catalog

obtained in this study (colored dots) color encoded with hypocentral depth. For reference, also relocated seismicity from the time period 2006-2016 after Wollin et al. (2018) is shown (black dots). In (a) and (b), temporary SMARTnet surface stations and permanent GONAF borehole vertical seismic arrays and strainmeter are indicated by yellow triangles and cyan squares, respectively. Location of earthquakes with M>4 since 2008 are marked with red stars (epicentral locations from AFAD catalog, focal mechanisms from Kinscher et al., (2013)). The purple star marks the estimated epicenter of the 1963 M 6.3 earthquake (Bulut and Aktar, 2007) together with its focal mechanism (Taymaz et al., 1991). Location of the M_W 5 aftershock of the 1999 M_W 7.4 Izmit earthquake in the Armutlu Peninsula is shown with a blue star, together with its focal mechanism (Pinar et al., 2003). Green star represents the location of the 2018 M_W 4.5 Esenkoy earthquake here analyzed.

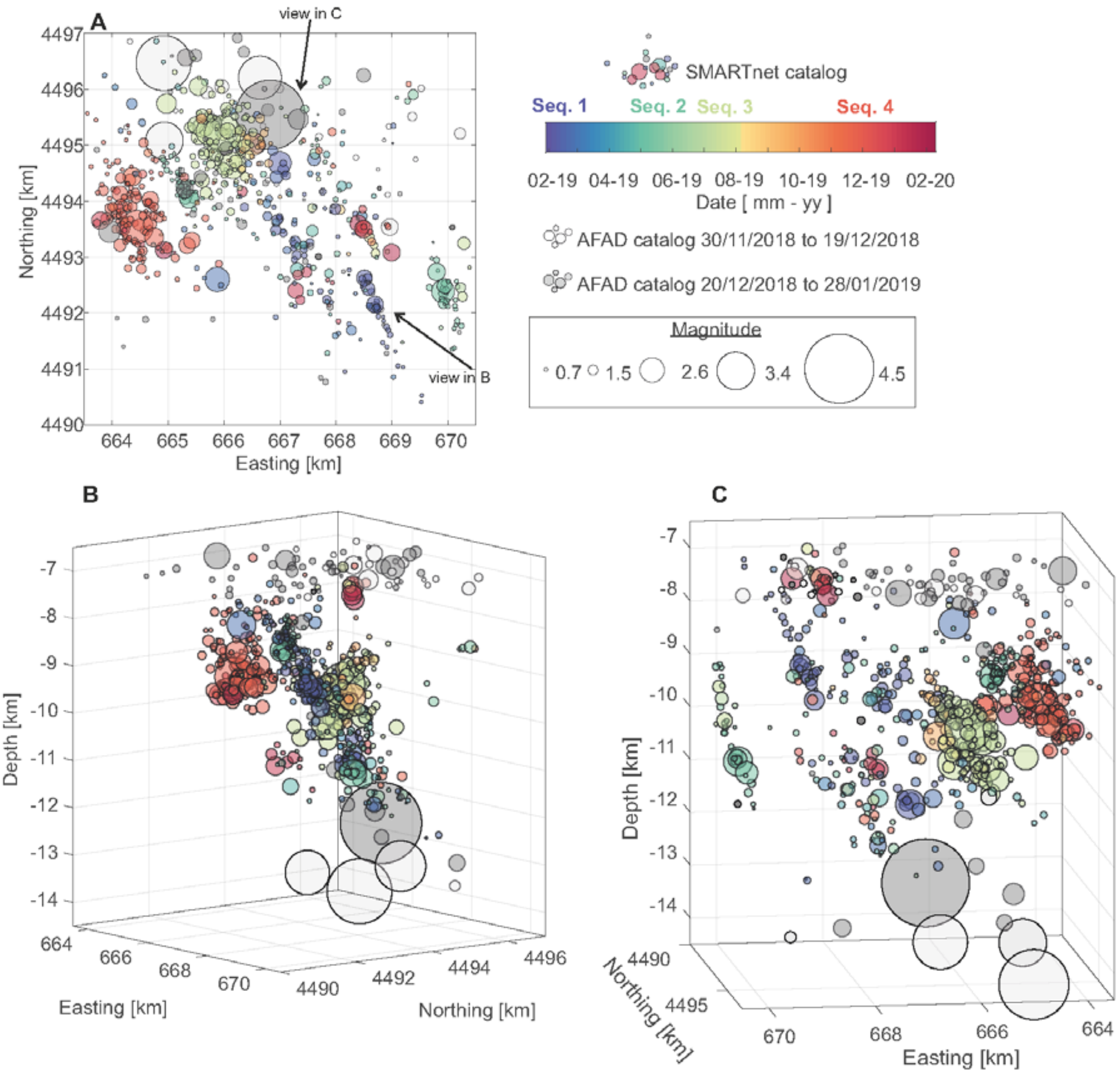

Figure 2: Seismically active area around the December 20th, 2018 M_W 4.5 Esenkoy earthquake (the biggest dark grey circle). Relocated seismicity from SMARTnet catalog is represented by colored circles, where color and circle size is encoded with origin time and magnitude, respectively. Grey circles represent the seismicity included in the catalog from the permanent Turkish network operated by AFAD for the time periods November 30th to December 19th, 2018 (light grey), and December 20th 2018 to January 28th, 2019 (dark grey) (a) Map view. (b) 3D view from an azimuth A = 126°, highlighting the roughly planar fault structure defined by the seismicity. (c) Same as (b) but from azimuth A = 8°. The color of the main four sequences described in the text appears marked in the colorbar.

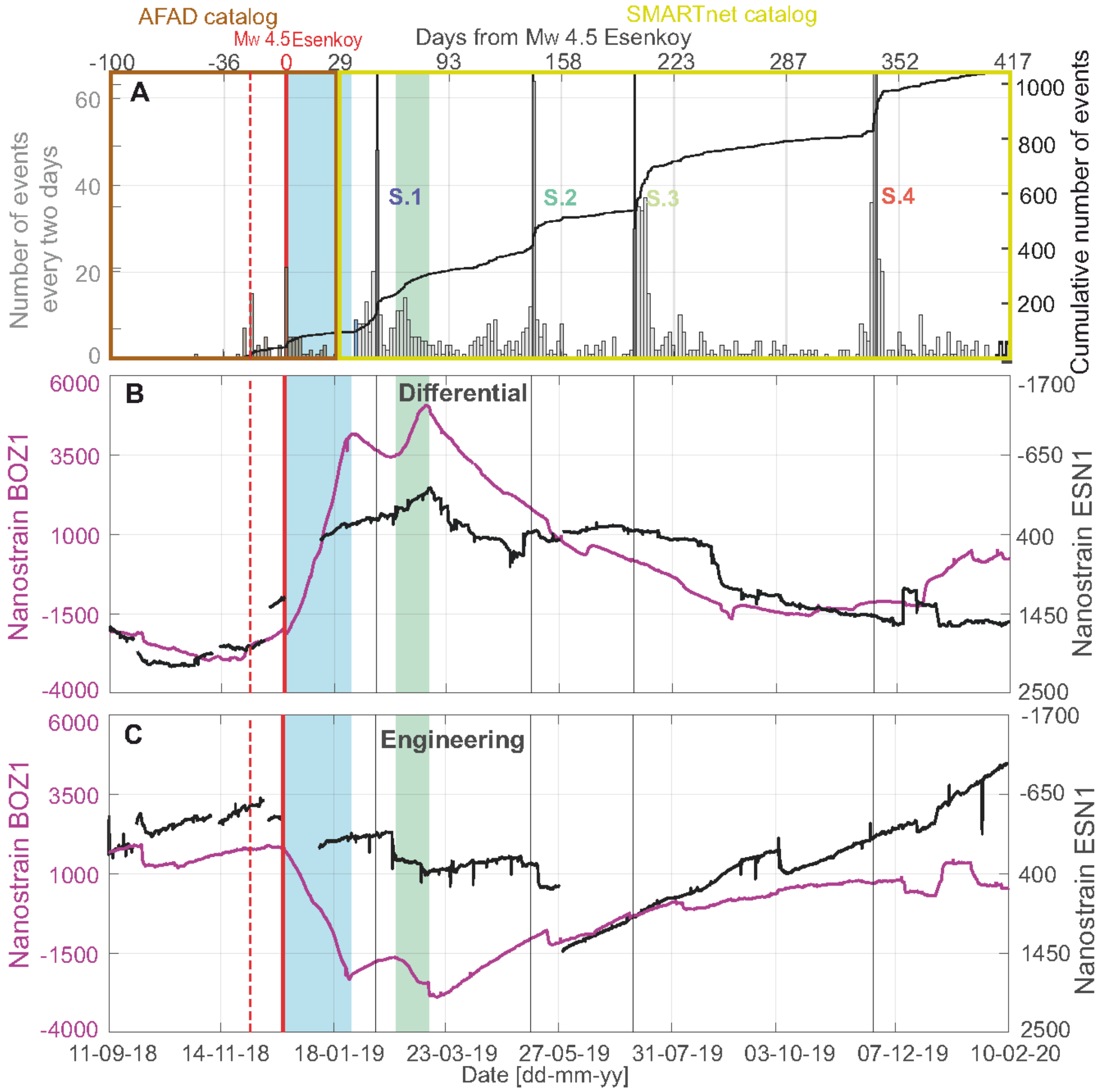

Figure 3: (a) Seismicity rates calculated every two days (grey bars) and cumulative number of events for the region analyzed here (see Figure 2 for spatial distribution) for a period of time covering 100 days before and 417 days after the 2018 M_W 4.5 Esenkoy earthquake. (b) Temporal evolution of differential components of strainmeter BOZ1 (in purple) and ESN1 (in black, note the reverted vertical scale). (c) Same as (b) but for the engineering component. In (a, b, c), origin time of the M_W 4.5 earthquake and a previous M_W 4.1 nearby are marked with red solid and dashed vertical lines, respectively. Black vertical lines represent the days with largest number of events for each of the four subsequent sequences. In all panels, light blue

rectangles represent the main transient signal observed, and light green panels represent a signal of similar trend only visible at BOZ1.

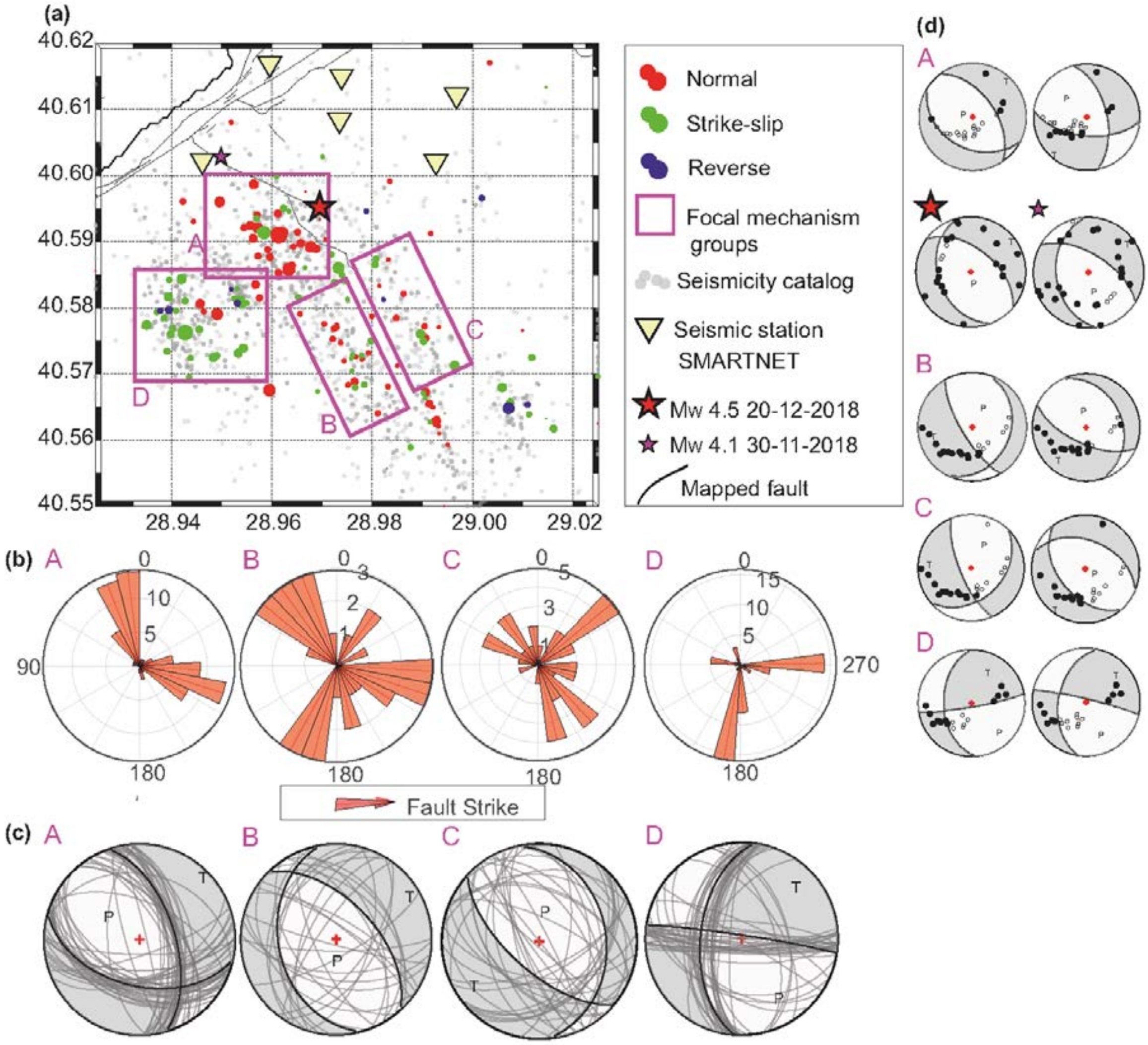

Figure 4: (a) Map view of the MT groups around the 2018 M_W 4.5 Esenkoy earthquake, with the estimated MTs color encoded according to their faulting style. The four groups for which hybridMT was applied are represented by purple rectangles. The Dec 20th 2018 M_W 4.5 and November 30th 2018 earthquakes are marked with a red and purple stars, respectively. (b) Rose diagrams showing polar histogram of fault strikes (including the two possible fault planes out of each solution). (c) Representation of average MT for each group (main beach balls), together

with all solutions from the corresponding group (grey lines). (d) Representative MTs from each group along with their station distribution over the focal sphere.

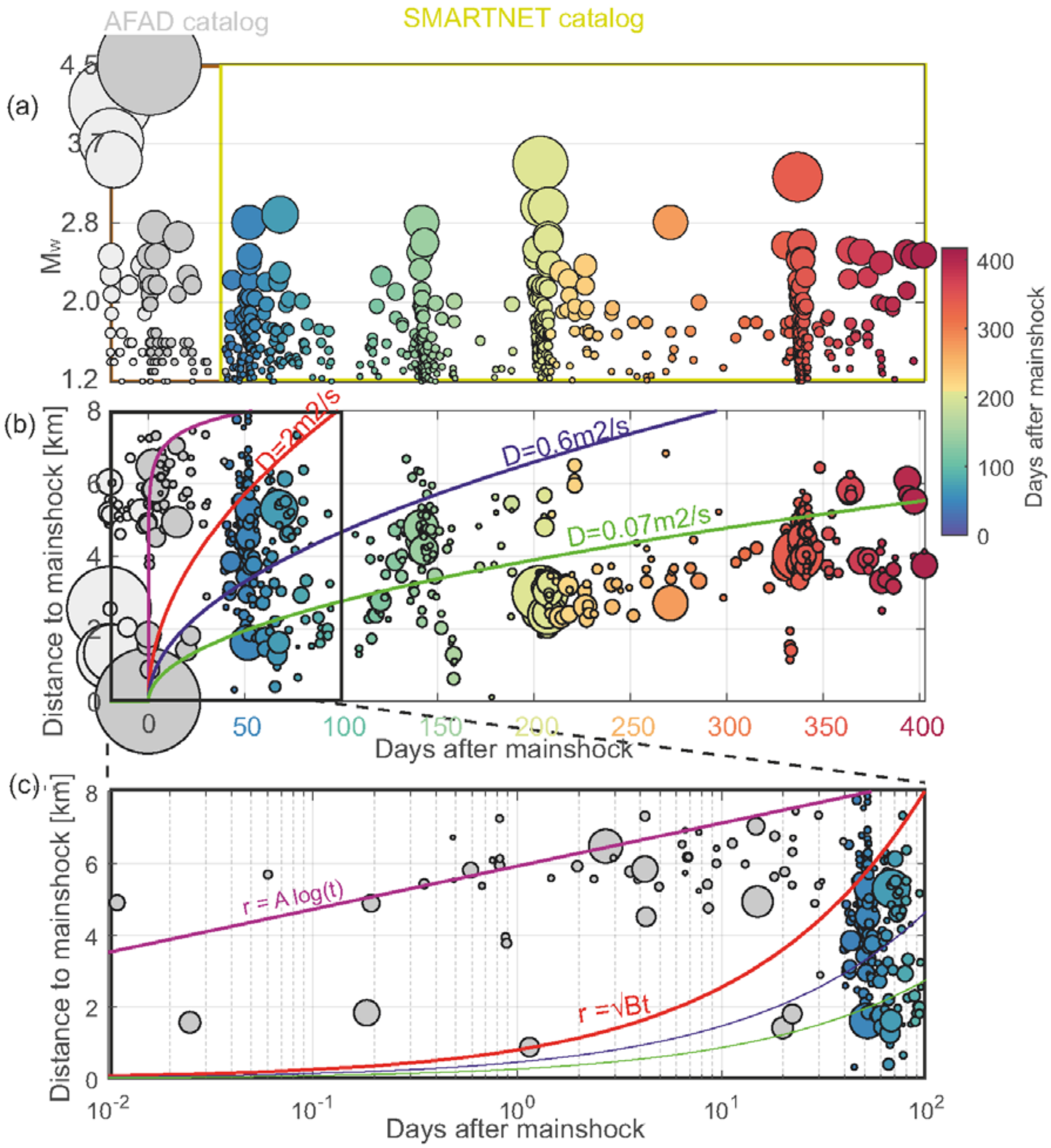

Figure 5: In-plane distance of the seismicity from the *M*w 4.5 Esenkoy earthquake (Dec 20th, 2018) versus time. Light and dark grey color represent seismicity from AFAD catalog before and after the *M*w 4.5 earthquake. Colored circles represent seismicity from SMARTnet which is color encoded with time. Symbol size is also encoded with moment magnitude (a) Magnitude distribution of the seismicity vs time. (b) In-plane distance between each seismic event and the

M_W 4.5 earthquake as a function of time.. Purple line indicates a seismicity migration front of the form $r = A \cdot log10(t)$, while the red, blue and green lines represent a fitting of the form r $= \sqrt{B \cdot t}$ for different diffusivity values. (c) Zoom-in focusing on the first 100 days after the M_W 4.5 earthquake, with the x axis in logarithmic scale.